

Acidic Polysaccharides as Green Alternatives for Barite Scale Dissolution

Ricardo D. Sosa,¹ Xi Geng,¹ Ankur Agarwal, Jeremy C. Palmer, Jacinta C. Conrad,*
Michael A. Reynolds,* and Jeffrey D. Rimer*



Cite This: *ACS Appl. Mater. Interfaces* 2020, 12, 55434–55443



Read Online

ACCESS |



Metrics & More



Article Recommendations



Supporting Information

ABSTRACT: Barium sulfate (barite) scale poses significant challenges for processes ranging from water treatment to fossil fuel production. Here, we identify alginate (a polysaccharide derived from brown algae) as a potent, “green” alternative to commercial barite demineralizing agents. Unlike conventional treatments of inorganic scales that require caustic conditions, alginate polymers dissolve barite at near-neutral conditions. In this study, we benchmark the demineralizing efficacy of alginate against a commercial dissolver, diethylenetriaminepentaacetic acid (DTPA), using a combination of bulk dissolution assays, scanning probe microscopy, and molecular dynamics simulations. Time-resolved rates of dissolution measured in a microfluidic device show that demineralization is enhanced more than an order of magnitude under flow. In situ atomic force microscopy reveals that alginate and DTPA exhibit distinct mechanisms of surface dissolution; and surprisingly, their binary combination in alkaline media results in a synergistic cooperativity that enhances the overall rate of barite dissolution. These studies collectively demonstrate a unique approach to demineralization using an inexpensive and abundant biopolymer that enables environmentally friendly treatment of inorganic scales.

KEYWORDS: crystallization, barium sulfate, microfluidics, atomic force microscopy, acidic polymer, mineral scale



INTRODUCTION

Crystallization of inorganic scales under flow conditions is often an undesirable and pervasive outcome of material transport in commercial wastewater treatment, manufacturing, and energy production. Progressive accumulation of mineral scale deposits can damage piping and equipment and cause pipeline blockage, resulting in production losses that negatively impact operations and the economics of industrial processes.^{1–3} Typical treatments for scale employ acid chemistry to drive the crystallization reaction in reverse and may include chelating agents to help solubilize the mineral scale. Remediation of acid-insoluble minerals such as barium sulfate (barite) rarely benefit from existing chemical treatments, thereby forcing industry to rely on costly mechanical methods for removal.

Chemical options for dissolving industrial scale include using chelating agents such as diethylenetriaminepentaacetic acid (DTPA), ethylenediaminepentaacetic acid (EDTA), and other aminopolycarboxylic acids.^{4–7} Although many studies have investigated the dissolution of barite with commercial additives (termed demineralizing agents),^{8–20} there is very little fundamental knowledge of dissolution mechanisms to aid in the rational design of new and improved alternatives. Moreover, commercial formulations used to treat barite scale require highly alkaline media (pH > 12),^{21,22} which has a

negative impact on the environment.²³ Therefore, it is advantageous to identify a new class of green (i.e., biodegradable) demineralizing agents and develop improved understanding of their modes of action to establish well-defined guidelines for the future design of scale dissolvers.^{24,25} More generally, this knowledge may also inform a broader spectrum of applications for applying organic growth modifiers to control crystallization, including (but not limited to) human diseases (e.g., kidney stones, malaria, and atherosclerosis) and biomineralization (e.g., bone, nacre, and coral).^{26–33}

Most demineralizing agents explored in the literature are small molecules. Some studies have shown evidence of synergistic cooperativity when combining a newly assayed demineralizing agent with either EDTA or DTPA.^{5,6,34} More recently, certain 18-membered macrocycles have been shown to be effective chelators of Ba²⁺ ions with efficiencies comparable to DTPA.³⁵ Studies have also shown that barite solubility is enhanced in the presence of bacteria, which is

Received: September 15, 2020

Accepted: November 10, 2020

Published: November 24, 2020



attributed to their putative generation of organic acids to chelate Ba^{2+} ions.³⁶

In contrast to small molecules, polymers potentially offer improved efficacy arising from the presence of multiple functional groups along the backbone. The use of polymeric demineralization agents has been investigated for calcite, another mineral commonly associated with scale formation. Studies of calcite crystallization in the presence of polyaspartic acid and alginate found that these polymers are effective demineralizing agents.^{37,38} By examining the macroscopic changes in crystals during bulk dissolution, these studies identified polymer specificity for distinct facets of calcite but were unable to provide a mechanistic understanding of their mode(s) of action at a molecular level. Alginate is of particular interest owing to its abundance in brown algae³⁹ and its extensive use in the food, pharmaceutical, and biomedical industries (e.g. as a gelling agent).^{40,41} Alginate is composed of mannuronic acid and guluronic acid residues, both of which participate in the gelling mechanism. Typically, two adjacent guluronic acid residues are reported to bind a single divalent cation through the formation of a buckling structure in the polymer, whereas mannuronic acid incorporation in the sequence reportedly provides flexibility to the polymer chain to facilitate gelation.⁴²

In this study, we test the hypothesis that multiple functional moieties of polysaccharides, including the acid and alcohol side groups of alginate and related analogues, are efficient binding groups for barite crystal surfaces. Comparison of seven biopolymers (both polysaccharides and their acid derivatives) reveals that alginate dissolves barite at rates much greater than other candidates. Moreover, direct comparison between alginate and DTPA shows that alginate has a greater efficacy in neutral media, whereas the combination of both demineralizing agents in alkaline media leads to synergistic cooperativity. The efficacy of barite dissolution is quantified at the macroscopic level using a microfluidic device that allows for the analysis of the average dissolution kinetics in the absence and presence of demineralizing agents, showing that the rates of dissolution can be markedly enhanced under flow conditions. These studies are complemented by in situ atomic force microscopy to probe specific interactions between the demineralizing agents and the crystal surfaces at a molecular level and to extract mechanistic details of their modes of action. These studies show that alginate is a highly efficient barite scale dissolver. Moreover, we uncover new insights for its potential replacement of long-standing commercial dissolvers.

RESULTS AND DISCUSSION

We examined a wide array of biopolymers (Figure 1) as potential green demineralizing agents for barite. The macromolecules selected for this study can be subdivided according to their primary functional groups: alcohols (I), carboxylates (II–IV), and sulfates (V–VII). Barite dissolution kinetics were assessed by time-resolved optical imaging of multiple single crystals under quiescent conditions and in a neutral (pH 7) medium containing an equal mass of each additive ($200 \mu\text{g mL}^{-1}$). Crystal dissolvers can be grouped into three categories based on their efficacy, as shown in Figure 1. The least effective polysaccharides identified in our measurements were carboxymethyl cellulose (II, where $R = \text{CH}_2\text{CO}_2\text{H}$, H, etc.), κ -carrageenan (V), and ι -carrageenan (VII). Three additives exhibited moderate efficacy: agarose (I), polygalacturonic acid

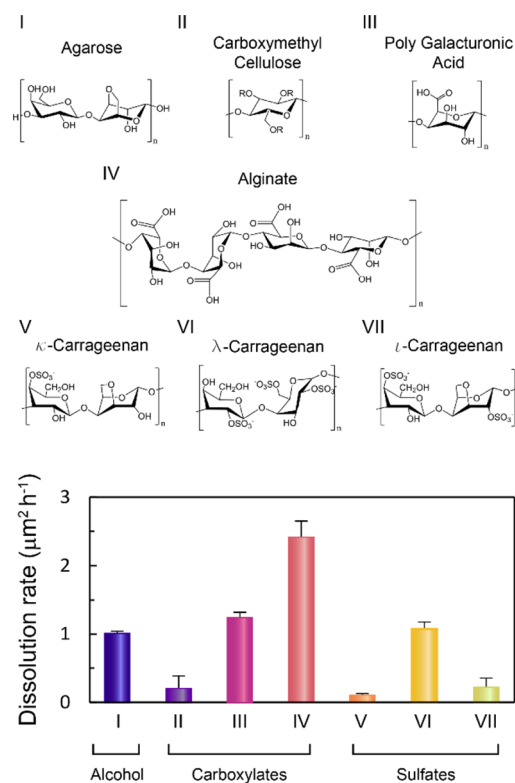


Figure 1. Bulk crystallization screening of potential barite dissolvers using macromolecules with polysaccharide backbones. (Top) List of molecules with (I) alcohol, (II–IV) carboxylate, and (V–VII) sulfate functional moieties. (Bottom) Rate of barite crystal dissolution in the presence of $200 \mu\text{g mL}^{-1}$ of additives in pH neutral aqueous media at $21 \pm 1 \text{ }^\circ\text{C}$ (quiescent conditions). Average dissolution rates were determined from three separate batches by measuring the crystal size over a 7-day period for at least 300 crystals (ca. 100 crystals per batch). Error bars equal one standard deviation.

(III), and λ -carrageenan (VI). Each of these molecules is decorated with chemically distinct binding groups ($-\text{OH}$, $-\text{COO}^-$, and $-\text{SO}_3^-$), indicating that all three functional moieties are influential in barite dissolution. Interestingly, only one of the polysaccharides, alginate (IV), was a standout in its ability to dissolve barite crystals. Alginate contains similar functional groups as polygalacturonic acid (i.e., alcohols and carboxylates); however, these molecules differ in their stereochemistry. Notably, alginate contains two monomers, mannuronic and guluronic acids, that alter the spatial distribution and orientation of the carboxylate functional groups interacting with barite crystal surfaces.

We examined the effect of alginate on barite dissolution in comparison with a commercial dissolver, DTPA, used as a benchmark. The kinetics of barite dissolution in the presence of $200 \mu\text{g mL}^{-1}$ of additives under neutral pH and quiescent conditions were measured using elemental analysis (ICP-MS) of the supernatant to track the release of Ba^{2+} ions over time (Figure 2a). The nonlinear dissolution profile of alginate is starkly in contrast to the nearly flat profile of DTPA. In the presence of alginate, the concentration of free Ba^{2+} ions increases rapidly at early times owing to the high degree of undersaturation but approaches a plateau at later times as the solution becomes saturated (the solubility product K_{sp} for barite at $25 \text{ }^\circ\text{C}$ is 1.08×10^{-10}).⁴³ The thermodynamic upper limit of free Ba^{2+} ions can be enhanced by the presence of

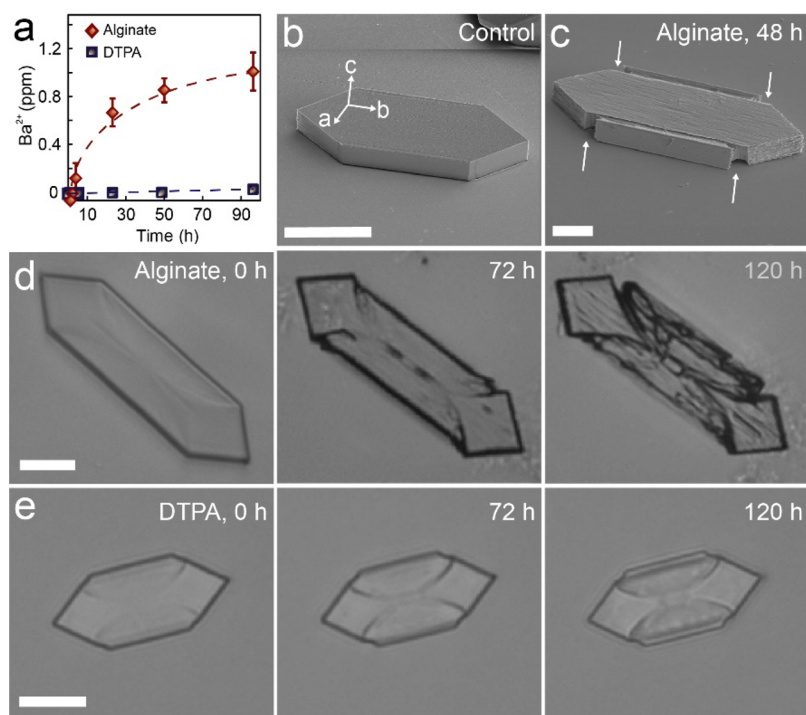


Figure 2. (a) Bulk assays of barite dissolution under quiescent conditions in a 20 mL vial at 21 ± 1 °C in the presence of $200 \mu\text{g mL}^{-1}$ of alginate (red diamonds) and DTPA (gray squares). The concentration of Ba^{2+} ions in the aliquots of the growth solution was measured periodically using ICP-MS. Each data point is an average of three measurements from different bulk dissolution assays, and error bars span two standard deviations. (b and c) Scanning electron micrographs of barite crystals (b) before and (c) after exposure to $200 \mu\text{g mL}^{-1}$ of alginate. The white arrows indicate the four corners where dissolution seemingly originates. (d and e) Optical micrographs of barite crystals in the presence of $200 \mu\text{g mL}^{-1}$ of (d) alginate solution and (e) DTPA solution under quiescent conditions over 5 days. Solutions used for all experiments were adjusted to pH 7. Scale bars equal $20 \mu\text{m}$.

chelating agents. Using a titration technique adapted from a reported protocol,³⁵ we confirmed that DTPA sequesters free Ba^{2+} ions from solution with a moderately better efficiency than alginate (Figure S1).

Barite crystals grown in the absence of additives exhibit a coffin-shape habit with basal {001}, side {100}, and apical {210} facets (Figure 2b). After exposure to alginate at neutral pH, barite dissolution is observed at the intersecting corners of the (100) and (210) faces, whereas the (001) surface displays striated etch pits elongated in the [010] direction (Figure 2c). Time-resolved optical images acquired during quiescent bulk dissolution over a 5-day period reveal anisotropic etching that seemingly originates from the corners of the barite crystal (Figure 2d). In the presence of DTPA at pH 7, we observe mild dissolution over a 5-day period leading to dissolution features originating from the corners (Figure 2e), similar to those observed for alginate.

It has been reported that the efficacy of DTPA as a barite dissolver is highly pH-dependent.^{12,17} DTPA is composed of five carboxylic acids ($\text{pK}_a = -0.1, 0.7, 1.6, 2.0,$ and 2.6) and three amine groups ($\text{pK}_a = 4.3, 8.6,$ and 10.5).⁴⁴ A speciation model (Figure 3a) shows that all five of its carboxylates are dissociated and all three of its amines remain in a free-base form (i.e., DTPA^{5-}) at high pH (>11), which is the most frequent condition employed in prior studies^{8–20} that examined the impact of DTPA^{5-} on barite dissolution. At neutral conditions, however, DTPA is zwitterionic. This property may explain its poor efficacy to dissolve barite under these conditions. For instance, the presence of positively charged amines can potentially lead to the formation of

intramolecular hydrogen bonds ($\text{C}_3\text{N}\cdots\text{H}\cdots\text{O}_2\text{C}$) that render acid groups on DTPA inaccessible for binding to barium sites on crystal surfaces. Alternatively, the positive charges on the amines may interact with sulfates on barite crystal surfaces, which have a net negative charge in aqueous media, as confirmed by zeta potential measurements (Figure S2).

To rationalize these observations, we performed umbrella sampling molecular dynamics (USMD) simulations^{46–48} to investigate the mechanism of DTPA-assisted detachment of Ba^{2+} ions from the barite (001) surface. The USMD simulations were used to compute the free energy surface (FES) associated with two coordination numbers (CNs), $\{\text{CN}_{\text{Ba}^{2+}-\text{S}}$ and $\text{CN}_{\text{Ba}^{2+}-\text{O}_{\text{DTPA}}}\}$, characterizing the extent of coordination of the central Ba^{2+} ion by S atoms in the barite crystal and by O atoms on DTPA's carboxyl groups (Figure 3b), respectively. Hence, regions in the FES where the values of $\text{CN}_{\text{Ba}^{2+}-\text{S}}$ and $\text{CN}_{\text{Ba}^{2+}-\text{O}_{\text{DTPA}}}$ are high and low, respectively, indicate that Ba^{2+} is strongly coordinated by sulfur atoms in barite and thus still attached to the crystal surface. Conversely, low values of $\text{CN}_{\text{Ba}^{2+}-\text{S}}$ and high values of $\text{CN}_{\text{Ba}^{2+}-\text{O}_{\text{DTPA}}}$ denote the states where Ba^{2+} is (partially) detached from the barite crystal and predominately coordinated in DTPA's carboxyl groups. The free energy calculations suggest that DTPA promotes detachment through several intermediate states. At pH 11, the fully detached state at $\{0.1, 3.6\}$ is at a lower free energy than the bound state at $\{>3.84, <2.75\}$, indicating that detachment is favorable. The detachment process is facilitated by partially unbound states at $\{2.9, 2.75\}$ and $\{1.9, 2.75\}$ (Figure 3b, (i) and (ii)) that are separated by low energy barriers (<5 kT), which can be overcome by

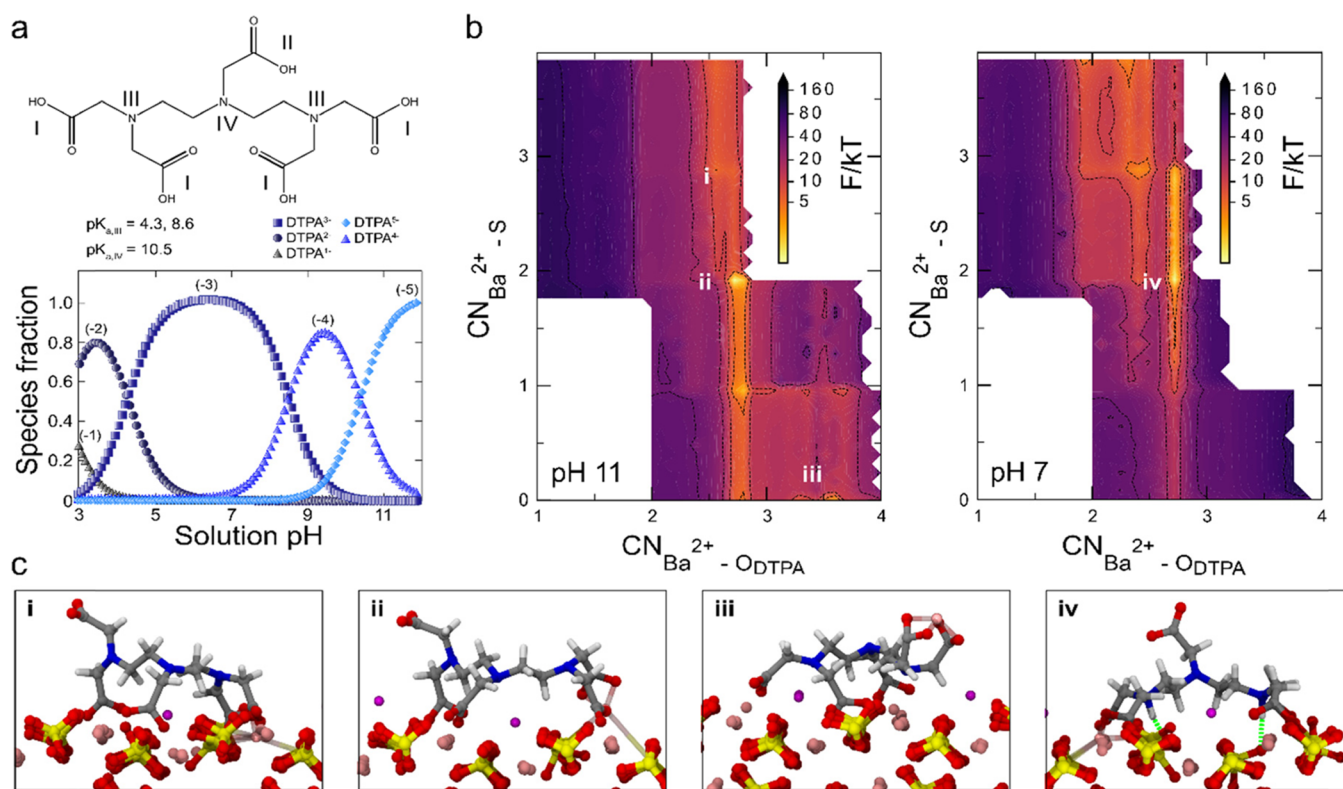


Figure 3. (a) (Top) Molecular structure of DTPA with the listed pKa values for the three amines (not listed: values for carboxylates are pKa_I = -0.1, 0.7, 1.6, and 2.0, and pKa_{II} = 2.6). The thermodynamic data were obtained from Moulin et al.⁴⁴ (Bottom) Speciation model for DTPAⁿ with labeled charges $n = -1$ to -5 corresponding to the sequential deprotonation of amines and carboxylic acids with increasing solution pH produced with the software package HySS2009.⁴⁵ (b) Free energy surfaces (FESs) from USMD simulations of DTPA-assisted detachment of Ba²⁺ ions from the barite (001) surface at pH 11 and 7 (left and right panels, respectively). The surfaces are parameterized by the coordination number (CN) of the central Ba²⁺ ion (x -axis) by O atoms on DTPA's carboxyl groups and by S atoms in the barite crystal (y -axis). (c) Representative configurations of DTPA from different regions on the FES illustrating the (i) attached and (iii) detached states of Ba²⁺ and (ii, iv) distinct intermediates observed at different pH conditions. The detached state (iii) is at the lower edge of the panel where CN_{Ba²⁺-S} ≈ 0 . Atoms are colored as follows: O (red), N (blue), C (gray), H (white), S (yellow), Ba²⁺ (pink), and Na⁺ (purple). Green lines denote h-bonds. Uncertainties in the FESs are approximately 1 kT.

thermal fluctuations. At pH 7, the stability of the intermediate state at {1.9,2.75} (Figure 3b, (iv)) is enhanced and there are relatively large free energy barriers (ca. 15 – 20 kT) along the pathways leading to complete detachment, implying slower detachment consistent with the slower dissolution rate observed in experiments. Inspection of the molecular configurations reveals that the state at {1.9,2.75} is stabilized at pH 7 by the formation of hydrogen (h)-bonds between DTPA's terminal amines and surface sulfate groups that are not present at pH 11 due to the deprotonation of the amine groups (Figure 3c, (iv); *Movies S1* and *S2*). These h-bonds inhibit the carboxylate group on DTPA from pulling away from the surface and thus detaching the coordinated Ba²⁺ ion.

Using an in situ microfluidic device, conditions such as solution flow rate, pH, and additive concentration were systematically varied to quantify their effect(s) on barite dissolution. In these studies, the change in the basal surface area (i.e., projected area measured normal to the (001) surface) was used to assess the rate of dissolution. First, measurements were performed over a range of flow rates (0–120 mL h⁻¹) and in the presence of 200 $\mu\text{g mL}^{-1}$ of additive (alginate or DTPA) at neutral pH. Consistent with observations under quiescent conditions, measurements under flow with DTPA showed little effect, whereas alginate increased the barite dissolution rate by approximately one

order of magnitude (Figure 4a). Measurements of the crystals in aqueous alginate solution revealed that the rate of barite dissolution increased proportionally with the flow rate until reaching a plateau at around 12 mL h⁻¹. This plateau indicates the transition from transport-limited to reaction-limited dissolution kinetics, similar to our previous study of barite growth.⁴⁹

Holding the flow rate fixed at 12 mL h⁻¹, the rate of barite dissolution was measured in microfluidic channels at varying solution pH (Figure 4b) for both additives. In the presence of 200 $\mu\text{g mL}^{-1}$ of DTPA, barite dissolution increased monotonically with increasing pH above pH 5. The effect of DTPA becomes noticeable once the pH reaches a value where the speciation model (Figure 3a) indicates appreciable quantities of DTPA⁴⁻ (pH 9) and DTPA⁵⁻ (pH 11). Conversely, alginate dissolves barite over a broader range of alkalinity (pH 3–7) where both mannuronic and guluronic acids are fully dissociated (pKa = 3.38 and 3.65, respectively).⁵⁰ Interestingly, we observed a reduction in barite dissolution at pH > 7 that cannot be easily rationalized. For instance, gel permeation chromatography (Figure S3) and infrared spectroscopy (Figure S4) do not show any evidence of alginate chemical degradation after incubation in highly alkaline media.^{51–53} Dynamic light scattering showed no evidence of alginate aggregation over a broad range of solution pH (Figure S5), and

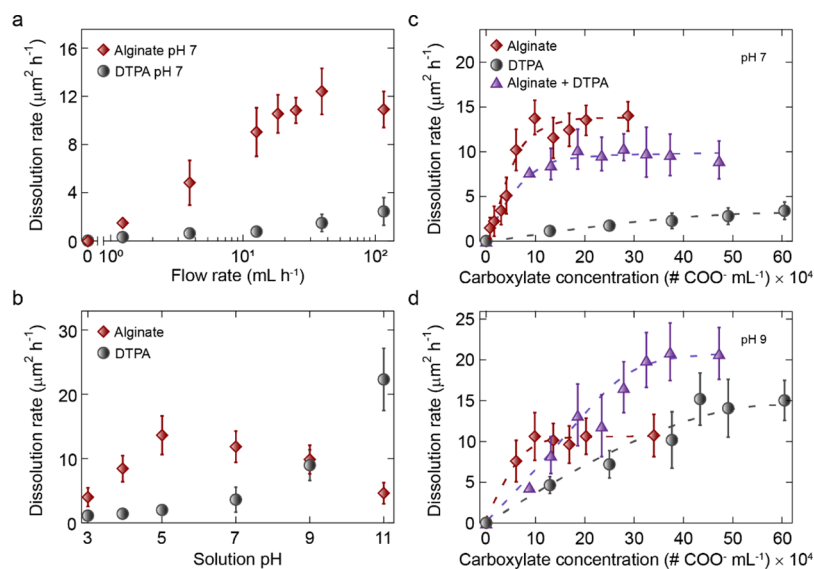


Figure 4. Microfluidic measurements of barite dissolution rate as a function of (a) flow rate (at pH 7) and (b) solution pH (at a constant flow rate of 12 mL h^{-1}). Dissolution rates were calculated based on the changes in the projected (001) surface area. Aqueous solutions of alginate and DTPA were prepared at $200 \mu\text{g mL}^{-1}$ of total additive concentration. Symbols represent the average measurements over at least 100 crystals for a single batch, and error bars span two standard deviations (note: error bars not visible are smaller than the size of the symbols). (c) Dissolution rate of barite as a function of total dissolver concentration in microchannels under a constant flow (12 mL h^{-1}) of solutions (pH 7) of alginate, DTPA, and 50/50 (wt %) alginate–DTPA binary mixtures. (d) Dissolution rate of barite in an alkaline solution (pH 9) under a constant flow (12 mL h^{-1}) in the presence of alginate, DTPA, and alginate–DTPA (50/50) binary mixtures. Additive concentrations are reported on the basis of acid site density. Symbols represent the average measurements of at least 100 crystals in a single batch, and error bars span two standard deviations. Dashed lines are interpolations to guide the eye.

bulk dissolution does not give any indication of unfavorable coverage effects such as repulsive adsorbate–adsorbate interactions (Figure 4c,d). Thus, alginate’s maximum efficacy is around pH 5 and the mechanism of its decline at higher pH remains elusive.

Prior studies of crystal growth inhibition have shown that binary combinations of additives can result in either synergistic or antagonistic cooperativity.^{54,55} Here, we examine the effect of using binary combinations of alginate and DTPA (50/50 by mass) on the rate of barite crystal dissolution at pH 7 (Figure 4c) and pH 9 (Figure 4d). To facilitate comparison, the concentration of each additive is reported with respect to the number of carboxylate (COO^-) groups for each dissolver cocktail. The general shape of the dissolution curves is characteristic of Langmuir adsorption, where an increase in the total additive concentration results in an increased rate of dissolution until reaching a plateau (i.e., concentrations corresponding to an approximate monolayer coverage of additive(s) on crystal surfaces). Although DTPA has little effect on the rate of dissolution at pH 7, its presence nevertheless influences alginate–barite interactions given that the binary combination results in an overall lower rate of dissolution compared to alginate as the sole dissolver. These results are indicative of a mild antagonistic cooperativity.

At pH 9, we observed an unusual switch from antagonistic cooperativity at low concentrations of binary dissolvers to synergistic cooperativity at higher concentrations (Figure 4d and Figure S6). This same trend does not hold at higher alkalinity (e.g., pH 12) where binary combinations result in extreme antagonistic cooperativity (Figure S7) owing to the decreased efficacy of alginate. Although DTPA and alginate exhibited similar rates of barite dissolution at pH 9, alginate reaches its maximum efficacy at a much lower concentration of

COO^- groups, indicating that it is a more potent dissolver than the commercial DTPA.

Ex situ images of barite crystals that have been partially dissolved in alginate under quiescent conditions reveal unique dissolution features. We first focus on the dissolution of (210) and (100) side facets, which are often overlooked in studies of barite dissolution and growth owing to the anisotropy of barite crystals that makes it difficult to image these surfaces. After 24 h of exposure to $200 \mu\text{g mL}^{-1}$ of alginate solution at neutral pH, scanning electron microscopy (SEM) images reveal highly rough (210) surfaces with visible protrusions (Figure 5a,b). To gain a molecular-level insight into the mechanism of dissolution, we performed in situ atomic force microscopy (AFM) studies on surfaces with exposed (210) surfaces. Time-resolved AFM images of these surfaces reveal highly corrugated steps (Figure 5c–e) with an average height of 3.8 \AA , corresponding to an approximate half unit cell dimension of barite. During continuous imaging, we observed layer-by-layer dissolution with each step receding at a constant rate (Movie S3 and Figure S8). Conversely, dissolution of the (100) surface occurs by a different mechanism. The (100) facet features rectangular etch pits of varying widths and depths exceeding 60 nm , as shown in the ex situ SEM images (Figure 5b, arrow) and AFM images (Figure 5f–h) of barite crystals partially dissolved in $200 \mu\text{g mL}^{-1}$ of alginate. The high density of etch pits on these surfaces makes in situ AFM measurements of the (100) facet challenging; thus, we report ex situ images that seem to indicate that alginate preferentially dissolves barite in the *a*- and *c*-directions.

Using in situ AFM, we measured barite dissolution under a constant flow (12 mL h^{-1}) for both the (001) and (210) surfaces. The results of the latter are described in the Supporting Information. Here, we focus on the basal (001) surface, where dissolution is more pronounced, and compare

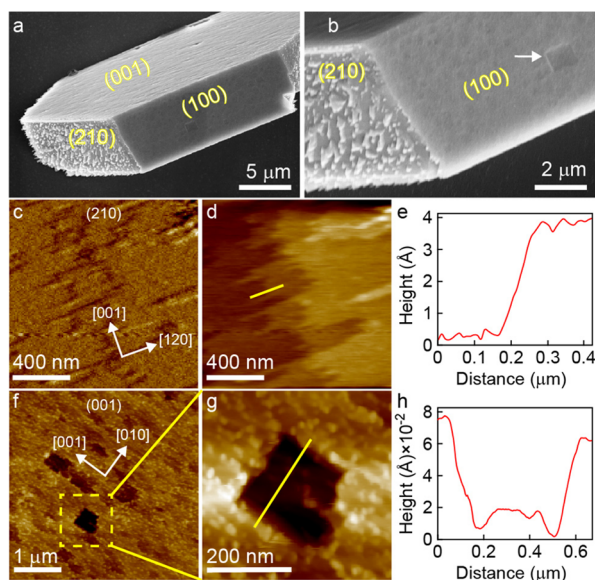


Figure 5. (a) Scanning electron micrograph of a barite crystal after 24 h dissolution (quiescent, pH 7) in the presence of $200 \mu\text{g mL}^{-1}$ of alginate. (b) Higher magnification SEM image showing the partially dissolved (210) facet and etch pits on the (100) facet of barite (arrow). (c–e) In situ measurements of the (210) surface dissolution under a constant flow rate of 12 mL h^{-1} aqueous solution at pH 7 containing $20 \mu\text{g mL}^{-1}$ of alginate. AFM deflection mode (c) and height mode (d) images extracted from [Movie S3](#) reveal 0.38 nm steps, as shown in the corresponding height profile (e) along the yellow line in (d). (f) Ex situ AFM deflection image of the (100) surface after exposure to $200 \mu\text{g mL}^{-1}$ of alginate (quiescent conditions, pH 7). A higher magnification of the area highlighted in the dashed box (g) shows a single etch pit with the corresponding height profile (h) along the solid yellow line.

our findings for four distinct solutions: (i) a control of $\text{NaOH}_{(\text{aq})}$ (pH = 9) without additives; (ii) the control modified by the addition of DTPA; (iii) an aqueous solution of alginate (pH = 7); and (iv) the control modified by the addition of alginate and DTPA (binary mixture). Time-resolved measurements of surface dissolution for the control revealed the birth and spread of triangular etch pits defined by the [010] and [120] directions ([Figure 6a,b](#) and [Figure S12](#)). A representative height profile of a partially dissolved surface shows etch pits with a depth of ca. 3.6 \AA ([Figure 6c](#)), which corresponds to a one-half unit cell dimension ($c/2$). In the presence of DTPA, the etch pits exhibit an elongated triangular morphology with rounded sides where the fastest rate of dissolution occurs in the [010] direction for etch pits bounded by the [130] and [010] edges ([Figure 6d,e](#) and [Figure S13](#)). The height profiles of these etch pits reveal identical depths (ca. 3.6 \AA , [Figure 6f](#)), indicating a layer-by-layer mechanism of dissolution. There is an inversion of etch pit orientation with each new layer owing to the 2_1 axis symmetry of barite with alternating sulfate group orientation between each half cell ([Figure S12](#)).^{11,15,56}

In the presence of alginate, the flat surface of the original barite substrate is indistinguishable within 12 min of exposure due to the rapid proliferation of etch pits ([Figure 6g,h](#)). These etch pits have ill-defined morphologies and do not appear to be bound by any crystallographic directions, in contrast to the triangular features observed for the control and the solution containing DTPA. Moreover, the height profiles of these etch pits ([Figure 6i](#)) reveal depths in excess of 50 \AA , corresponding

to more than seven unit cells. Etch pits appear randomly on the surface and become more elongated in the [010] direction, similar to DTPA. These results reveal that alginate dissolves barite by etching along the b -direction and into the (001) surface (c -direction). Although the sequence of events that occur during alginate-mediated dissolution is not yet identified, we posit that this unique mechanism may be facilitated by the ability of the flexible polymeric backbone of alginate and its many binding groups to interact with multiple Ba^{2+} ions in a concerted manner.

We also probed the cooperative synergy between alginate and DTPA for surface dissolution via AFM experiments using binary combinations where the solution was adjusted to pH 9. Barite crystals exposed to binary combinations of DTPA and alginate exhibit a distribution of etch pit depths and diameters ([Figure 6j–m](#)). A fraction of etch pits exhibit 3.6 \AA ($c/2$) depth profiles ([Figure S13](#)), while the majority of etch pits are much deeper (10 \AA or larger) and tend to have tiered profiles that are composed of macrosteps ([Figure 6l](#)). The cooperative synergy appears to be associated with the ability of alginate to create newly exposed layers and the preferential dissolution of layers within the plane of imaging by DTPA, as illustrated in [Figure 6m](#). This observed dual action of cooperative dissolvers leads to an overall rough (001) surface that is more similar to the single component solution of alginate compared to that of DTPA.

CONCLUSIONS

The dissolution of barite using natural, biocompatible additives at moderate pH has been underexplored. Through screening a series of polysaccharides, we identified alginate as an efficient alternative to DTPA. Using a combination of bulk dissolution assays and molecular dynamics, we show that DTPA is only active as a barite demineralizing agent at high pH owing to lower energetic barriers for its removal of Ba^{2+} ions from crystal surfaces. Microfluidic assays of barite dissolution under flow reveal a marked increase in the rate of barite dissolution compared to quiescent conditions. These studies demonstrate a high efficacy of alginate over a broad range of solution pH (4–9) relative to DTPA (pH ≥ 9). In situ AFM measurements reveal that alginate and DTPA exhibit distinct modes of dissolution, and a binary combination of these two demineralizing agents in alkaline media results in synergistic cooperativity. On a molecular level, AFM imaging of the (001) barite surface reveals that alginate induces deep ($>50 \text{ \AA}$) etch pits in the c -direction. Conversely, DTPA promotes layer-by-layer dissolution in the a/b -plane to generate shallow etch pits. For binary mixtures of alginate and DTPA, the origin of synergy derives from the fact that the two demineralizing agents promote dissolution in orthogonal directions, which enhances the overall rate of barite dissolution.

In many natural and synthetic crystallization processes, organics play a pivotal role in regulating crystal growth and dissolution. This is particularly true in biomineralization where materials, such as calcium carbonates and phosphates, grow into exquisite hierarchical structures via highly specific organic–crystal interactions. Designing molecules to promote dissolution is desirable for cases where mineralization is unwanted or detrimental, such as barite (and other scale) formation in confined aqueous flow regimes, as well as numerous pathological diseases. Few studies in the literature have elucidated molecular-level mechanisms of mineral dissolution at the solvent–crystal interface. Here, we do so

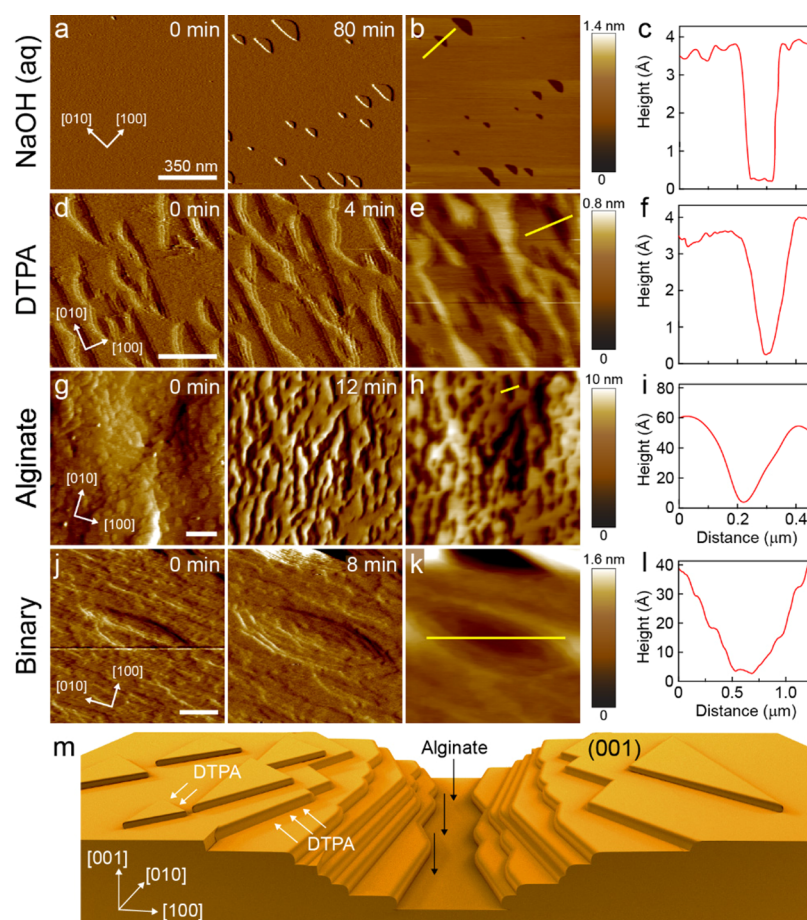


Figure 6. In situ AFM measurements of barite (001) surface dissolution in different media (see also [Movies S4–S7](#)). Time-elapsing deflection mode images in the solution of (a) NaOH (pH 9, control), (d) $200 \mu\text{g mL}^{-1}$ of DTPA (pH 9), (g) $200 \mu\text{g mL}^{-1}$ of alginate (pH 7), and (j) a binary combination of $100 \mu\text{g mL}^{-1}$ of DTPA and $100 \mu\text{g mL}^{-1}$ of alginate (pH 9). Corresponding height images after the specified exposure time are provided in (b), (e), (h), and (k). Height profiles of etch pits along the yellow lines of each height mode image are shown in (c), (f), (i), and (l), respectively. (m) Idealized scheme of binary dissolution where alginate preferentially dissolves in the *c*-direction and DTPA promotes layer recession in the *a*- and *b*-directions.

for a newly identified naturally abundant and environmentally compatible biopolymer. These findings collectively demonstrate alginate's versatility and efficacy as a demineralizing agent. Further studies to identify its mechanism of action and to characterize its effectiveness in a range of environmental conditions (temperature and pressure) will speed up the use of alginate in formulations to treat barite (and potentially other scale) formation.

METHODS

Barite Crystallization and Characterization. Barite crystals were prepared using a previously reported protocol.⁴⁹ A 5 mL solution of 1.2 M $\text{NaCl}_{(\text{aq})}$ was first added into a 20 mL glass vial followed by 0.5 mL aliquot addition each of 10 mM $\text{BaCl}_{2(\text{aq})}$ and 10 mM $\text{Na}_2\text{SO}_{4(\text{aq})}$ stock solutions. To this solution was added 4 mL of deionized (DI) water under mild agitation for 10 s to produce a growth solution (10 mL) with a composition of 0.5 mM BaCl_2 :0.5 mM Na_2SO_4 :600 mM NaCl (pH = 7.1 ± 0.3). The pH of the growth solutions was measured using an Orion 3-Star Plus pH benchtop meter equipped with a ROSS Ultra electrode (8102BNUWP). The sample vials were left undisturbed at $22 \pm 1 \text{ }^\circ\text{C}$ for 24 h to allow crystallization of hexagonal barite platelets with well-defined (001), (210), and (100) facets (see [Figure 2b](#)). Natural barite samples were obtained from Amazon. The zeta potential ζ of natural and synthetic barite samples was measured with a NICOMP 380/ZLS instrument (Particle Sizing Systems, Santa Barbara, CA).

Dissolution Assays under Quiescent Conditions. Demineralizing agent stock solutions were prepared by the addition of 40 mg of the reagent to 200 mL of DI water followed by pH neutralization with an appropriate amount of 100 mM $\text{NaOH}_{(\text{aq})}$. After 24 h of crystallization, the supernatant was removed using a pipette and barite crystals adhered to the bottom of the 20 mL glass vials were rinsed in DI water in triplicate. Immediately after rinsing the crystals, 20 mL aliquots of demineralizing agents ($200 \mu\text{g mL}^{-1}$) were introduced into the glass vials containing the barite seed crystals and were left undisturbed for 7 days.

In a separate experiment intended for ex situ imaging, a clean glass slide ($1 \times 1 \text{ cm}^2$) was placed at the bottom of a 20 mL glass vial prior to the addition of reagents used for barite crystallization. Immediately after synthesis, the glass slide containing the newly formed barite crystals was removed from the supernatant and rinsed thoroughly in DI water and dried in air. The slide was then positioned at the bottom of a vial containing 20 mL of a selected demineralizing agent solution ($200 \mu\text{g mL}^{-1}$). Barite crystals were exposed to solutions for 1–10 days. The glass slide was removed from the solution and rinsed in DI water and dried in air.

Dissolution Assays under Flow Conditions. The details of the microfluidic platform and procedures used to measure the in situ rates of crystal dissolution under constant flow were described in a previous study.⁴⁹ The dissolution of barite was performed in solutions of varying pH that were prepared by adding appropriate amounts of $\text{NaOH}_{(\text{aq})}$ or $\text{HCl}_{(\text{aq})}$ to DI water. The flow configuration for carrying out barite dissolution (described in detail in our previous study⁴⁹)

included a dual syringe pump that fed two separate solutions, one containing DI water and the other containing $500 \mu\text{g mL}^{-1}$ of a demineralizing agent, into the respective inlets of the microchannels.

The barite crystal size and morphology were determined using a Leica DMi8 inverted optical microscope equipped with HC PL Fluotar 5X, 10X, and 20X and N Plan L 50X objectives. At least 10 bright-field images of representative areas on the bottom of the glass vials were captured in the transmittance mode for characterization of crystals dissolved in polysaccharide solutions. The average basal surface area of barite crystals in optical micrographs was measured from a minimum of 100 crystals per batch and three separate batches. An inverted optical microscope equipped with a motorized stage was used to image the crystals in the bulk crystallization assays as well as time-resolved demineralization in microfluidics assays. For in situ time-resolved studies, the LAS X software was used to program a minimum of 15 positions along a seeded microchannel. Images were captured in the transmittance mode at 5 min intervals for a minimum of 3 h. Crystals observed in situ were analyzed using ImageJ (NIH) with a protocol previously reported.⁴⁹ At least 100 crystals located in different channels in a single batch were analyzed at 5 min intervals over a minimum of 3 h. From the change in the crystal basal (001) surface area over time, a dissolution rate r was calculated for each experimental condition as $r_{\text{dissolution}} = \Delta S_A t^{-1}$, where ΔS_A is the change in the (001) surface area and t is the time (in hours).

Scanning Electron Microscopy. Ex situ microscopy measurements were obtained using an FEI 235 dual-beam focused ion beam SEM. For SEM imaging, a clean glass slide ($1 \times 1 \text{ cm}^2$) was positioned at the bottom of the bulk crystallization vials to collect barite crystals. Samples containing either the as-synthesized crystals or those after dissolution assays were removed from their native solutions, gently rinsed with DI water, and dried in air prior to the analysis. SEM samples were prepared by attaching the glass slides to SEM studs (Ted Pella) using carbon tape and were coated with 15–20 nm gold to reduce electron beam charging.

Atomic Force Microscopy. All AFM measurements were performed with a Cypher ES instrument (Asylum Research, Santa Barbara, CA) using silicon nitride probes with a gold reflex coating and a spring constant of 0.08 N m^{-1} (Olympus, PNP-TR). The liquid cell (ES-CELL-GAS) contained two ports for inlet and outlet flow to maintain constant composition during continuous imaging. Barite crystals prepared via bulk crystallization (described above) were synthesized directly onto an AFM specimen disk (Ted Pella) covered with a thin layer of thermally curable epoxy (Loctite, China). The epoxy was first partially cured in an oven for ca. 5 min at $60 \text{ }^\circ\text{C}$ prior to drying in air overnight to completely cure. The AFM specimen disks were placed at the bottom of the 20 mL glass vials, and reagents used for bulk crystallization of barite were subsequently introduced to the vials upon which crystals nucleated, sedimented onto the epoxy, and grew overnight. The samples were gently rinsed with DI water and dried in air for one hour prior to imaging.

For ex situ imaging of the (100) surface of barite, glass slides containing barite crystals used in quiescent dissolution assays were fixed onto an AFM specimen disk using epoxy and left undisturbed overnight to allow the epoxy to fully cure. These samples were imaged in air at an ambient temperature in contact mode with a scan rate of 2.44 Hz at 256 lines per scan. In situ AFM measurements of barite dissolution were carried out by introducing a growth solution with a composition of 0.06 mM BaCl_2 and 0.06 mM Na_2SO_4 (supersaturation ratio $S = 5.3$) in DI water into the fluid cell using an in-line mixing configuration at a flow rate of 12 mL h^{-1} to obtain a smooth (001) surface with classical growth features. Measurements were performed using several concentrations of aqueous NaOH, alginate, and DTPA solutions (pH = 7–9) that were introduced into the fluid cell following a 30 min growth period. Continuous imaging was carried out at an ambient temperature in contact mode with a scan rate of 9.77 Hz at 256 lines per scan.

Molecular Dynamics Simulations. Molecular dynamics (MD) simulations were conducted with GROMACS 2016.^{57,58} Barite was described using the force field developed by Piana et al.,⁵⁹ DTPA was modeled using GROMOS force-field parameters from the Automatic

Topology Builder (ATB) server,⁶⁰ and the SPC model⁶¹ was used for water. Water–barite interactions were described using the force field of Piana et al.'s study,⁵⁹ and standard geometric mixing rules were used to parameterize all other van der Waals interactions, with parameters for O and S in barite from ATB and parameters for Ba from Rowley et al.'s study.⁶² USMD simulations were performed using the PLUMED 2.4.3^{63,64} plugin for GROMACS to characterize the DTPA-assisted detachment of Ba^{2+} ions from the barite (001) surface. Additional details of the MD simulations are provided in the Supplementary Methods section within the Supporting Information.

■ ASSOCIATED CONTENT

Supporting Information

The Supporting Information is available free of charge at <https://pubs.acs.org/doi/10.1021/acsami.0c16653>.

Zeta potential measurements of barite crystals; gel permeation chromatograph, FTIR spectra, and dynamic light scattering measurements of alginate solutions; optical micrographs of barite crystals during dissolution; and in situ AFM images and data analysis (PDF)

Visualization of a 7.5 ns MD trajectory of DTPA at pH 11 (DTPA^{5-}) at the barite (001) surface, viewed along the [010] direction (MP4)

Visualization of a 7.5 ns MD trajectory of DTPA at pH 7 (DTPA^{3-}) at the barite (001) surface, viewed along the [010] direction (MP4)

Time-elapased sequence of AFM deflection mode images depicting the dissolution of the (210) barite surface in $20 \mu\text{g mL}^{-1}$ of alginate solution at pH 7 in the absence of Ba^{2+} and SO_4^{2-} ions (AVI)

Time-elapased sequence of AFM deflection mode images depicting the dissolution of the (001) barite surface in $10 \mu\text{M}$ NaOH solution (pH 9) in the absence of Ba^{2+} and SO_4^{2-} ions (AVI)

Time-elapased sequence of AFM deflection mode images depicting the dissolution of the (001) barite surface in $200 \mu\text{g mL}^{-1}$ of DTPA solution (pH 9) in the absence of Ba^{2+} and SO_4^{2-} ions (MP4)

Time-elapased sequence of AFM deflection mode images depicting the growth of the (001) barite surface initially under flow of a supersaturated growth solution (supersaturation ratio $S = 7$) and subsequent dissolution in $200 \mu\text{g mL}^{-1}$ of alginate solution (pH 7) in the absence of Ba^{2+} and SO_4^{2-} ions (AVI)

Time-elapased sequence of AFM deflection mode images depicting the dissolution of the (001) barite surface in a solution containing $100 \mu\text{g mL}^{-1}$ of alginate and $100 \mu\text{g mL}^{-1}$ of DTPA (pH 9) in the absence of Ba^{2+} and SO_4^{2-} ions (AVI)

■ AUTHOR INFORMATION

Corresponding Authors

Jacinta C. Conrad – Department of Chemical and Biomolecular Engineering, University of Houston, Houston, Texas 77204-4004, United States; orcid.org/0000-0001-6084-4772; Email: jconrad@uh.edu

Michael A. Reynolds – Shell Exploration and Production Company, Houston, Texas 77079, United States; orcid.org/0000-0002-0900-1400; Email: Mike.Reynolds@shell.com

Jeffrey D. Rimer – Department of Chemical and Biomolecular Engineering, University of Houston, Houston, Texas 77204-

4004, United States; orcid.org/0000-0002-2296-3428;
Email: jrimer@central.uh.edu

Authors

Ricardo D. Sosa – Department of Chemical and Biomolecular Engineering, University of Houston, Houston, Texas 77204-4004, United States

Xi Geng – Department of Chemical and Biomolecular Engineering, University of Houston, Houston, Texas 77204-4004, United States

Ankur Agarwal – Department of Chemical and Biomolecular Engineering, University of Houston, Houston, Texas 77204-4004, United States

Jeremy C. Palmer – Department of Chemical and Biomolecular Engineering, University of Houston, Houston, Texas 77204-4004, United States; orcid.org/0000-0003-0856-4743

Complete contact information is available at:
<https://pubs.acs.org/10.1021/acsami.0c16653>

Author Contributions

[†]These authors contributed equally

Notes

The authors declare no competing financial interest.

ACKNOWLEDGMENTS

We acknowledge the financial support from Shell Oil Company (Award C112839). R.D.S. received support from the National Science Foundation Graduate Student Fellowship program (Award DGE 1144207). J.D.R., J.C.C., and J.C.P. also acknowledge support from the Welch Foundation (Awards E-1794, E-1869, and E-1882, respectively).

REFERENCES

- (1) Hanor, J. S. Barite–Celestine Geochemistry and Environments of Formation. *Rev. in Mineral. and Geochem.* **2000**, *40*, 193–275.
- (2) Li, J.; Tang, M.; Ye, Z.; Chen, L.; Zhou, Y. Scale Formation and Control in Oil and Gas Fields: A Review. *J. Dispersion Sci. Technol.* **2017**, *38*, 661–670.
- (3) Mike Crabtree, D. E. Phil Fletcher, Matt Miller, Ashley Johnson, King George, *Fighting Scale - Removal and Prevention*. *Oilfield Review* **1999**, 30–45.
- (4) Mason, D.J., Composition for Removing Naturally Occurring Radioactive Material (NORM) Scale. 2018, US 9,896,615.
- (5) Morris, R.L.; Paul, J.M., Sulfate Scale Dissolution. 1992, US 5,084,105.
- (6) D'muhala, T.F., Barium Sulfate Removal and Anti-Deposition Compositions and Process of Use Therefor. 1987, US 4,708,805.
- (7) De Jong, R., Torny-Schutte, G.J., Reinhoudt, D.N., Dissolving Barium Sulfate Scale with Aqueous Solutions of Salts of Carboxymethyl Monocyclic Macroyclic Polyamines. 1980, US 4,215,000.
- (8) Bageri, B. S.; Mahmoud, M. A.; Shawabkeh, R. A.; Al-Mutairi, S. H.; Abdulraheem, A. Toward a Complete Removal of Barite (Barium Sulfate BaSO₄) Scale Using Chelating Agents and Catalysts. *Arab. J. Sci. and Engineer.* **2017**, *42*, 1667–1674.
- (9) Dunn, K.; Yen, T. F. Dissolution of Barium Sulfate Scale Deposits by Chelating Agents. *Environ. Sci. Technol.* **1999**, *33*, 2821–2824.
- (10) Kowacz, M.; Putnis, C. V.; Putnis, A. The Control of Solution Composition on Ligand-Promoted Dissolution: Dtpa–Barite Interactions. *Cryst. Growth Des.* **2009**, *9*, 5266–5272.
- (11) Putnis, A.; Junta-Rosso, J. L.; Hochella, M. F. Dissolution of Barite by a Chelating Ligand: An Atomic Force Microscopy Study. *Geochim. Cosmochim. Acta* **1995**, *59*, 4623–4632.
- (12) Putnis, A., Putnis, C.V., Paul, J.M., The Efficiency of a DTPA-Based Solvent in the Dissolution of Barium Sulfate Scale Deposits, In *SPE International Symposium on Oilfield Chemistry*. Society of Petroleum Engineers: San Antonio, Texas, 1995 13.
- (13) Putnis, C. V.; Kowacz, M.; Putnis, A. The Mechanism and Kinetics of DTPA-Promoted Dissolution of Barite. *Appl. Geochem.* **2008**, *23*, 2778–2788.
- (14) Bao, H. Purifying Barite for Oxygen Isotope Measurement by Dissolution and Reprecipitation in a Chelating Solution. *Anal. Chem.* **2006**, *78*, 304–309.
- (15) Bosbach, D.; Hall, C.; Putnis, A. Mineral Precipitation and Dissolution in Aqueous Solution: In-Situ Microscopic Observations on Barite (001) with Atomic Force Microscopy. *Chem. Geol.* **1998**, *151*, 143–160.
- (16) Dunn, K.; Daniel, E.; Shuler, P. J.; Chen, H. J.; Tang, Y.; Yen, T. F. Mechanisms of Surface Precipitation and Dissolution of Barite: A Morphology Approach. *J. Colloid Interface Sci.* **1999**, *214*, 427–437.
- (17) Lakatos, I., Lakatos-Szabo, J., Kosztin, B.. Optimization of Barite Dissolvers by Organic Acids and pH Regulation. In *International Symposium on Oilfield Scale*; Society of Petroleum Engineers, 2002.
- (18) Lakatos, I., Lakatos-Szabo, J., Kosztin, B.. Comparative Study of Different Barite Dissolvers: Technical and Economic Aspects. In *International Symposium and Exhibition on Formation Damage Control*; Society of Petroleum Engineers, 2002.
- (19) Shen, D.; Fu, G.; Al-Saiari, H. A.; Kan, A. T.; Tomson, M. B. Barite Dissolution/Precipitation Kinetics in Porous Media and in the Presence and Absence of a Common Scale Inhibitor. *SPE Journal* **2013**, *14*, 462–471.
- (20) Wang, K.-S.; Resch, R.; Dunn, K.; Shuler, P.; Tang, Y.; Koel, B. E.; Yen, T. F. Dissolution of the Barite (001) Surface by the Chelating Agent DTPA as Studied with Non-Contact Atomic Force Microscopy. *Colloids Surf, A* **1999**, *160*, 217–227.
- (21) Abdelgawad, K., Mahmoud, M., Elkhatny, S., Patil, S.. Effect of Calcium Carbonate on Barite Solubility Using a Chelating Agent and Converter. In *SPE International Conference on Oilfield Chemistry*; Society of Petroleum Engineers, 2019.
- (22) Morris, R.L.; Paul, J.M., Method for Removing Alkaline Sulfate Scale. 1990, US 4,980,077.
- (23) Means, J. L.; Kucak, T.; Crerar, D. A. Relative Degradation Rates of NTA, EDTA and DTPA and Environmental Implications. *Environ. Pollu. Series B, Chem. and Phys.* **1980**, *1*, 45–60.
- (24) Harry, D.; Horton, D.; Durham, D.; Constable, D. J. C.; Gaffney, S.; Moore, J.; Todd, B.; Martinez, I. Grand Challenges and Opportunities for Greener Chemical Alternatives in Hydraulic Fracturing: A Perspective from the ACS Green Chemistry Institute Oilfield Chemistry Roundtable. *Energy Fuels* **2020**, *34*, 7837–7846.
- (25) Reynolds, M. A. A Technical Playbook for Chemicals and Additives Used in the Hydraulic Fracturing of Shales. *Energy Fuels* **2020**, No. 0c02527.
- (26) Addadi, L.; Berman, A.; Moradian-Oldak, J.; Weiner, S. Tuning of Crystal Nucleation and Growth by Proteins: Molecular Interactions at Solid-Liquid Interfaces in Biomineralization. *Croat. Chem. Acta* **1990**, *63*, 539–544.
- (27) Aizenberg, J. Crystallization in Patterns: A Bio-Inspired Approach. *Adv. Mater.* **2004**, *16*, 1295–1302.
- (28) Aizenberg, J.; Lambert, G.; Weiner, S.; Addadi, L. Factors Involved in the Formation of Amorphous and Crystalline Calcium Carbonate: A Study of an Ascidian Skeleton. *J. Am. Chem. Soc.* **2002**, *124*, 32–39.
- (29) De Yoreo, J. J.; Gilbert, P. U.; Sommerdijk, N. A.; Penn, R. L.; Whitelam, S.; Joester, D.; Zhang, H.; Rimer, J. D.; Navrotsky, A.; Banfield, J. F. Crystallization by Particle Attachment in Synthetic, Biogenic, and Geologic Environments. *Science* **2015**, *349*, aaa6760.
- (30) Dove, P.M., De Yoreo, J.J., Weiner, S., *Biomineralization*. Vol. 54; Walter de Gruyter GmbH & Co KG, 2018.
- (31) Smeets, P. J.; Cho, K. R.; Kempen, R. G.; Sommerdijk, N. A.; De Yoreo, J. J. Calcium Carbonate Nucleation Driven by Ion Binding

in a Biomimetic Matrix Revealed by in Situ Electron Microscopy. *Nat. Mater.* **2015**, *14*, 394–399.

(32) Tambutté, S.; Holcomb, M.; Ferrier-Pagès, C.; Reynaud, S.; Tambutté, É.; Zoccola, D.; Allemand, D. Coral Biomineralization: From the Gene to the Environment. *J. Experiment. Marine Biol. and Ecol.* **2011**, *408*, 58–78.

(33) Weiner, S.; Addadi, L. Crystallization Pathways in Biomineralization. *Annu. Rev. Mater. Res.* **2011**, *41*, 21–40.

(34) Paul, J.; Fieler, E. A New Solvent for Oilfield Scales. In *SPE Ann. Techn. Confer. and Exhib.*; Society of Petroleum Engineers, 1992.

(35) Thiele, N. A.; MacMillan, S. N.; Wilson, J. J. Rapid Dissolution of BaSO₄ by Macropa, an 18-Membered Macrocyclic with High Affinity for Ba²⁺. *J. Am. Chem. Soc.* **2018**, *140*, 17071–17078.

(36) Ouyang, B.; Akob, D. M.; Dunlap, V.; Renock, D. Microbially Mediated Barite Dissolution in Anoxic Brines. *Appl. Geochem.* **2017**, *76*, 51–59.

(37) Perry, T. D., IV; Duckworth, O. W.; McNamara, C. J.; Martin, S. T.; Mitchell, R. Effects of the Biologically Produced Polymer Alginic Acid on Macroscopic and Microscopic Calcite Dissolution Rates. *Environ. Sci. Technol.* **2004**, *38*, 3040–3046.

(38) Burns, K.; Wu, Y.-T.; Grant, C. S. Mechanisms of Calcite Dissolution Using Environmentally Benign Polyaspartic Acid: A Rotating Disk Study. *Langmuir* **2003**, *19*, 5669–5679.

(39) Lee, O. K.; Lee, E. Y. Sustainable Production of Bioethanol from Renewable Brown Algae Biomass. *Biomass Bioenergy* **2016**, *92*, 70–75.

(40) Ching, S. H.; Bansal, N.; Bhandari, B. Alginate Gel Particles—a Review of Production Techniques and Physical Properties. *Critic. Rev. in Food Sci. and Nutri.* **2016**, *57*, 1133–1152.

(41) Tam, S.; Bilodeau, S.; Dusseault, J.; Langlois, G.; Hallé, J.-P.; Yahia, L. Biocompatibility and Physicochemical Characteristics of Alginate–Polycation Microcapsules. *Acta Biomater.* **2011**, *7*, 1683–1692.

(42) Onsoyen, E., Alginates, in *Thickening and Gelling Agents for Food*. 1997, Springer. 22–44.

(43) Blount, C. W. Barite Solubilities and Thermodynamic Quantities up to 300 °C and 1400 Bars. *Am. Mineral.* **1977**, *62*, 942–957.

(44) Moulin, C.; Amekraz, B.; Steiner, V.; Plancque, G.; Ansoborlo, E. Speciation Studies on DTPA Using the Complementary Nature of Electrospray Ionization Mass Spectrometry and Time-Resolved Laser-Induced Fluorescence. *Appl. Spectrosc.* **2016**, *57*, 1151–1161.

(45) Alderighi, L.; Gans, P.; Ienco, A.; Peters, D.; Sabatini, A.; Vacca, A. J. C. Hyperquad Simulation and Speciation (HySS): A Utility Program for the Investigation of Equilibria Involving Soluble and Partially Soluble Species. *Coord. Chem. Rev.* **1999**, *184*, 311–318.

(46) Palmer, J. C.; Debenedetti, P. G. Recent Advances in Molecular Simulation: A Chemical Engineering Perspective. *AIChE J.* **2015**, *61*, 370–383.

(47) Qin, W.; Agarwal, A.; Choudhary, M. K.; Palmer, J. C.; Rimer, J. D. Molecular Modifiers Suppress Nonclassical Pathways of Zeolite Crystallization. *Chem. Mater.* **2019**, *31*, 3228–3238.

(48) Torrie, G. M.; Valleau, J. P. Nonphysical Sampling Distributions in Monte Carlo Free-Energy Estimation: Umbrella Sampling. *J. Comput. Phys.* **1977**, *23*, 187–199.

(49) Sosa, R. D.; Geng, X.; Reynolds, M. A.; Rimer, J. D.; Conrad, J. C. A Microfluidic Approach for Probing Hydrodynamic Effects in Barite Scale Formation. *Lab Chip* **2019**, *19*, 1534–1544.

(50) Chuang, J.-J.; Huang, Y.-Y.; Lo, S.-H.; Hsu, T.-F.; Huang, W.-Y.; Huang, S.-L.; Lin, Y.-S. Effects of pH on the Shape of Alginate Particles and Its Release Behavior. *Inter. J. Polymer Sci.* **2017**, *2017*, 1.

(51) Gómez-Ordóñez, E.; Rupérez, P. FTIR-ATR Spectroscopy as a Tool for Polysaccharide Identification in Edible Brown and Red Seaweeds. *Food Hydrocolloids* **2011**, *25*, 1514–1520.

(52) Papageorgiou, S. K.; Kouvelos, E. P.; Favvas, E. P.; Sapalidis, A. A.; Romanos, G. E.; Katsaros, F. K. Metal–Carboxylate Interactions in Metal–Alginate Complexes Studied with FTIR Spectroscopy. *Carbohydr. Res.* **2010**, *345*, 469–473.

(53) Sarmiento, B. Characterization of Insulin-Loaded Alginate Nanoparticles Produced by Iontropic Pre-Gelation through DSC and FTIR Studies. *Carbohydr. Polym.* **2006**, *66*, 1–7.

(54) Ma, W.; Lutsko, J. F.; Rimer, J. D.; Vekilov, P. G. Antagonistic Cooperativity between Crystal Growth Modifiers. *Nature* **2020**, *577*, 497–501.

(55) Farmanesh, S.; Ramamoorthy, S.; Chung, J.; Asplin, J. R.; Karande, P.; Rimer, J. D. Specificity of Growth Inhibitors and Their Cooperative Effects in Calcium Oxalate Monohydrate Crystallization. *J. Am. Chem. Soc.* **2013**, *136*, 367–376.

(56) Hill, R. A Further Refinement of the Barite Structure. *Canad. Mineral.* **1977**, *15*, 522–526.

(57) Abraham, M., Van der Spoel, D., Lindahl, E., Hess, B., *The Gromacs Development Team (2018) Gromacs User Manual*, Version 2016.

(58) Abraham, M. J.; Murtola, T.; Schulz, R.; Páll, S.; Smith, J. C.; Hess, B.; Lindahl, E. Gromacs: High Performance Molecular Simulations through Multi-Level Parallelism from Laptops to Supercomputers. *SoftwareX* **2015**, *1-2*, 19–25.

(59) Piana, S.; Jones, F.; Gale, J. D. Assisted Desolvation as a Key Kinetic Step for Crystal Growth. *J. Am. Chem. Soc.* **2006**, *128*, 13568–13574.

(60) Malde, A. K.; Zuo, L.; Breeze, M.; Stroet, M.; Poger, D.; Nair, P. C.; Oostenbrink, C.; Mark, A. E. An Automated Force Field Topology Builder (ATB) and Repository: Version 1.0. *J. Chem. Theory Comput.* **2011**, *7*, 4026–4037.

(61) Berendsen, H.J.; Postma, J.P., van Gunsteren, W.F., Hermans, J., Interaction Models for Water in Relation to Protein Hydration. In *Intermolecular Forces*; Springer, 1981, pp. 331–342.

(62) Rowley, C. N.; Roux, B. A Computational Study of Barium Blockades in the KcsA Potassium Channel Based on Multi-Ion Potential of Mean Force Calculations and Free Energy Perturbation. *J. General Physiol.* **2013**, *142*, 451–463.

(63) Bonomi, M.; Branduardi, D.; Bussi, G.; Camilloni, C.; Provasi, D.; Raiker, P.; Donadio, D.; Marinelli, F.; Pietrucci, F.; Broglia, R. A. PLUMED: A Portable Plugin for Free-Energy Calculations with Molecular Dynamics. *Comput. Phys. Commun.* **2009**, *180*, 1961–1972.

(64) Tribello, G. A.; Bonomi, M.; Branduardi, D.; Camilloni, C.; Bussi, G. PLUMED 2: New Feathers for an Old Bird. *Comput. Phys. Commun.* **2014**, *185*, 604–613.